New insights into the $D_{s0}^*(2317)$ and other charm scalar mesons

Zhi-Hui Guo,[1,2,*] Ulf-G. Meißner,[3,4,†] and De-Liang Yao[4,‡]

[1]*Department of Physics, Hebei Normal University, Shijiazhuang 050024, People's Republic of China*
[2]*State Key Laboratory of Theoretical Physics, Institute of Theoretical Physics, CAS, Beijing 100190,*
People's Republic of China
[3]*Helmholtz-Institut für Strahlen- und Kernphysik and Bethe Center for Theoretical Physics,*
Universität Bonn, D–53115 Bonn, Germany
[4]*Institute for Advanced Simulation, Institut für Kernphysik and Jülich Center for Hadron Physics,*
Forschungszentrum Jülich, D-52425 Jülich, Germany

Through the scattering of light-pseudoscalar mesons (π, K, η, η') off charmed mesons (D, D_s), we study the $D_{s0}^*(2317)$ state and other relevant charm scalar mesons in a unitarized chiral effective field theory approach. We investigate the charm scalar meson poles with different strangeness (S) and isospin (I) quantum numbers as well as their corresponding residues, which provide the coupling strengths of the charm scalar mesons. Both the light-quark mass and N_C dependences of the pole positions of the $D_{s0}^*(2317)$ and the poles with $(S, I) = (0, 1/2)$ are analyzed in detail in this work. Interestingly we observe quite similar pion mass trajectories for the resonance pole at around 2.1 GeV with $(S, I) = (0, 1/2)$ to those of the $f_0(500)$ given in the literature. When increasing the values of N_C we find that a bound state and a virtual state in the $(S, I) = (1, 0)$ channel asymmetrically approach the DK threshold for $N_C < 6$, and they meet at this threshold at $N_C = 6$. When $N_C > 6$, the bound and virtual states move into the complex plane on the second Riemann sheet and become a symmetric pair of resonance poles. For large enough values of N_C, neither the $D_{s0}^*(2317)$ pole nor the poles with $(S, I) = (0, 1/2)$ tend to fall down to the real axis, indicating that they do not behave like a standard quark-antiquark meson at large N_C.

I. INTRODUCTION

The discovery of the scalar charmed-strange meson $D_{s0}^*(2317)$ [1–3] has triggered intensive studies in hadron physics. With its mass just about 40 MeV below the DK threshold, it is one of the few precious examples of a loosely bound state observed in the meson sector. The scattering of the charmed and light pseudoscalar mesons provides a powerful tool to probe the inner structure of $D_{s0}^*(2317)$. Recently much progress from lattice simulations focusing on the $D_{s0}^*(2317)$ state has been made investigating the previously mentioned scattering processes [4–7]. The pion masses used in these lattice simulations are still large compared to the physical value, so the chiral extrapolations are necessary to obtain physical predictions from the lattice data. Chiral perturbation theory (χPT), as an effective field theory of low energy QCD, has been demonstrated to be a successful and reliable tool to perform the chiral extrapolations in many lattice simulations [8].

In traditional heavy meson χPT (HMχPT), proposed by Refs. [9–11], not only is the chiral symmetry encoded but also the heavy-quark symmetry is complemented so as to study heavy-light systems. Due to the incorporation of

heavy-quark symmetry, the interactions are independent of heavy-quark spin and flavor, which imply that the scalar D and vector D^* should be treated as counterparts to form, for instance, a spin doublet. However, following Ref. [12], a covariant HMχPT, in combination only with the chiral symmetry, will be imposed to investigate the interactions between the charmed D and pseudo-Nambu-Goldstone bosons (pNGBs) in this work. In covariant χPT, the necessity of the inclusion of the D^* relies on the size of its contributions. In our case, only the 0^+ charmed states involved in the S-wave interactions will be studied and the vector D^* only contributes via u-channel exchange, which provides a negligible contribution to the interacting potential at tree level [13]. Therefore we consider it is a good approximation to exclude the vector D^* mesons when focusing only on the S-wave charmed D meson and pNGB scattering. Within the framework of covariant heavy meson χPT by taking the $D_{(s)}$ and the octet of pNGBs as the dynamical fields, the leading order (LO) [14–16], next-to-leading order (NLO) [12,13,17–19] and next-to-next-to-leading order (NNLO) [20,21] calculations have been performed to investigate the properties of $D_{s0}^*(2317)$. The pole trajectories with varying up/down- and strange-quark masses are useful quantities to further probe the inner structure of the hadrons, e.g., the M_π and M_K dependences of $D_{s0}^*(2317)$ have been extensively studied in previous Refs. [13,18,19] and similar trajectories for the light-flavor

*zhguo@mail.hebtu.edu.cn
†meissner@hiskp.uni-bonn.de
‡d.yao@fz-juelich.de

resonances $f_0(500)/\sigma$ and $\rho(770)$ are predicted in Refs. [22,23]. Another kind of pole trajectories with varying N_C, with N_C the number of colors in QCD, has been demonstrated to be useful to discriminate different explanations for light-flavor resonances [24–28], such as for $f_0(500)$, $\rho(770)$, etc. However, the study of the N_C trajectories of the $D_{s0}^*(2317)$ state is still lacking. One of the key novelties of the present work is to fill this gap. The N_C trajectories for other pertinent charm scalar mesons resulting from the $D_{(s)}$ and pNGBs scattering shall be investigated as well. We note that finite-volume corrections for this type of scattering processes have recently been worked out, see Refs. [29,30].

We point out that in order to study the N_C trajectories of the poles from the $D_{(s)}$ and pNGBs scattering, it is inappropriate to only consider the $SU(3)$ octet of pNGBs, i.e., π, K, η_8. The singlet η_0 becomes a relevant degree of freedom (d.o.f) when discussing large N_C. The reason is that the QCD $U(1)_A$ anomaly, which is responsible for the massive η_0 in the physical case at $N_C = 3$, is $1/N_C$ suppressed in the large N_C limit. As a result, the QCD spectrum is the pNGB nonet at low energy in the chiral and large N_C limits [31–34], rather than the $SU(3)$ octet resulting in the chiral limit. Therefore it is necessary for us to generalize the previous discussions on the charmed mesons $D_{(s)}$ and the pNGB octet scattering, such as those in Refs. [12–16,18,19,21], to the processes involving the singlet η_0. After the inclusion of the singlet η_0, not only the QCD spectrum is completed in the large N_C limit, but also we can have a more realistic description for the physical η meson at $N_C = 3$, since the physical η and η' mesons are mixtures of η_8 and η_0. While in the standard $SU(3)$ χPT, the η_8 is typically identified with the physical η state [35] and $\eta - \eta'$ mixing effects appear in certain low energy constants (LECs), in particular in L_7. Within the χPT framework with explicit light pseudoscalar octet plus singlet π, K, η, η' (recognized as large N_C or $U(3)$ χPT [36]) and the charmed mesons $D_{(s)}$, we give an updated discussion by taking into account the lattice simulations and pay special attention to the pole spectra in the scattering of light pseudoscalar and charmed mesons.

The paper is organized as follows. We first calculate all of the amplitudes for the charmed meson (D, D_s) and light pseudoscalars (π, K, η, η') scattering processes in $U(3)$ χPT, and then we use a simple recipe to unitarize the perturbative scattering amplitudes. This will be the main focus of Sec. II. The fits to the lattice simulation data will be presented in Sec. III, where we determine all of the free parameters. The pole contents, the corresponding residues and the pole trajectories with varying light-quark masses and N_C will be analyzed in detail in Sec. IV. Finally, we give a summary and conclude in Sec. V.

II. CHIRAL AMPLITUDES AND THEIR UNITARIZATION

Due to inclusion of the singlet η_0, with its mass squared M_0^2 remaining massive even in the chiral limit and behaving

as $1/N_C$ for $N_C \to \infty$, one needs to introduce the $1/N_C$ expansion together with conventional chiral expansion consisting of soft momentum squared p^2 and light-quark masses m_q, in order to strictly establish a consistent power-counting [36,37]. The simultaneous triple expansions on the soft momentum squared, light-quark masses and $1/N_C$, i.e., $\mathcal{O}(\delta) \sim \mathcal{O}(p^2) \sim \mathcal{O}(m_q) \sim \mathcal{O}(1/N_C)$, will change the hierarchy of some operators assigned by the conventional chiral power counting. Typical examples are $L_4\langle u_\mu u^\mu\rangle\langle\chi_+\rangle$ and $L_5\langle u_\mu u^\mu\chi_+\rangle$ from the light flavor $SU(3)$ χPT. Although the operators accompanying L_4 and L_5 belong to the same order in the $SU(3)$ case, their orders are changed in the triple-expansion scheme when the singlet η_0 is introduced [36], since they have different orders in $1/N_C$. Compared to the $SU(3)$ octet case, new operators in the $U(3)$ case with arbitrary number of the building block $X = \langle\ln\det U\rangle \propto \eta_0$ term can appear [37], with U the matrix of the pNGBs. However, from large N_C argument, one more X field introduces one more order of the $1/N_C$ suppression. Therefore, the new operators with extra terms of the X field are more suppressed by $1/N_C$. On the other hand, from the practical point of view, the operators with the X term exclusively contribute to the processes involving η and η' mesons, which are only relevant to the coupled channels of the $D_{(s)}$ and pNGBs scattering. While the present lattice simulations in the coupled channel case are still rare and bear large uncertainties, as shown in later discussions, it is still not possible to make sensible determinations of the LECs accompanied by the new operators with the X term. Moreover, since the singlet η_0 predominantly contributes to the physical η' state, the contributions from the new operators with an X term will mainly enter the channels involving the η' meson, which have thresholds that are obviously higher than in the other channels. This further indicates the irrelevance of the operators with an X term in the present work. So we shall stop including any operator beyond the NLO discussion in Refs. [12,13,18,19], which also enables us to make clear comparisons with the previous results.

The LO Lagrangian that describes the interactions between the charmed-meson triplet $\mathcal{P} = (D^0, D^+, D_s^+)$ and pNGBs takes the form

$$\mathcal{L}_{\mathcal{P}\phi}^{(1)} = \mathcal{D}_\mu\mathcal{P}\mathcal{D}^\mu\mathcal{P}^\dagger - \overline{M}_D^2\mathcal{P}\mathcal{P}^\dagger, \tag{1}$$

which also provides the kinetic terms for the charmed mesons. The quantity $\overline{M}_D$ stands for the mass of the charmed mesons in the chiral limit. The covariant derivative $\mathcal{D}_\mu$ acting on the charmed mesons $\mathcal{P}$ is given by

$$\mathcal{D}_\mu\mathcal{P} = \mathcal{P}(\overset{\leftarrow}{\partial}_\mu + \Gamma_\mu^\dagger), \qquad \mathcal{D}_\mu\mathcal{P}^\dagger = (\partial_\mu + \Gamma_\mu)\mathcal{P}^\dagger, \tag{2}$$

where

$$\Gamma_\mu = \frac{1}{2}[u^\dagger(\partial_\mu - ir_\mu)u + u(\partial_\mu - i\ell_\mu)u^\dagger], \qquad u^2 = U = e^{i\frac{\sqrt{2}\Phi}{F}},$$

$$\Phi = \begin{pmatrix} \frac{1}{\sqrt{2}}\pi^0 + \frac{1}{\sqrt{6}}\eta_8 + \frac{1}{\sqrt{3}}\eta_0 & \pi^+ & K^+ \\ \pi^- & -\frac{1}{\sqrt{2}}\pi^0 + \frac{1}{\sqrt{6}}\eta_8 + \frac{1}{\sqrt{3}}\eta_0 & K^0 \\ K^- & \overline{K}^0 & \frac{-2}{\sqrt{6}}\eta_8 + \frac{1}{\sqrt{3}}\eta_0 \end{pmatrix}. \tag{3}$$

In the above equations, r_μ and ℓ_μ denote the right- and left-hand external sources. F denotes the weak decay constant of the pNGBs in the chiral and large N_C limits, with the normalization $F_\pi = 92.2$ MeV. A clear difference in the present discussion, compared to the previous ones in Refs. [12–16,18,19,21], is the inclusion of the singlet η_0 in pNGB matrix given in Eq. (3).

The NLO Lagrangian that generalizes Eq. (1) reads [12]

$$\mathcal{L}_{\mathcal{P}\phi}^{(2)} = \mathcal{P}(-h_0\langle\chi_+\rangle - h_1\chi_+ + h_2\langle u_\mu u^\mu\rangle - h_3 u_\mu u^\mu)\mathcal{P}^\dagger + \mathcal{D}_\mu\mathcal{P}(h_4\langle u_\mu u^\nu\rangle - h_5\{u^\mu, u^\nu\})\mathcal{D}_\nu\mathcal{P}^\dagger, \tag{4}$$

with

$$\chi_+ = u^\dagger\chi u^\dagger + u\chi^\dagger u,$$
$$u_\mu = i\{u^\dagger(\partial_\mu - ir_\mu)u - u(\partial_\mu - u\ell_\mu)u^\dagger\}, \tag{5}$$

where $\chi = 2B(s + ip)$ includes the scalar (s) and pseudoscalar (p) external sources. The quantity B is related to the light-quark condensate via $\langle 0|\overline{q}^i q^j|0\rangle = -F^2 B\delta^{ij}$ at leading order. The light-quark masses in χPT are introduced by taking $(s + ip) = \text{diag}(\hat{m}, \hat{m}, m_s)$, with $\hat{m}$ the average up and down quark mass and m_s the strange quark mass. Isospin violating effects will not be considered throughout this work. Though in the strict triple expansion of $U(3)$ χPT the LECs in Eq. (4) belong to different orders, we simply quote them as the NLO ones as in Refs. [12,21], since no other new operators with additional X field will be considered and in this way it enables us to make clear comparisons with the results in the literature.

The relevant chiral Lagrangian with only the pNGB d.o.f is given by [31–33,36,37]

$$\mathcal{L}_\chi = \frac{F^2}{4}\langle u_\mu u^\mu\rangle + \frac{F^2}{4}\langle\chi_+\rangle + \frac{F^2}{12}M_0^2 X^2, \tag{6}$$

with $X = \ln(\det U)$. At leading order, the physical η and η' can be obtained through the diagonalization of the η_0 and η_8 states in Eq. (6), and they are related by

$$\begin{pmatrix} \eta \\ \eta' \end{pmatrix} = \begin{pmatrix} c_\theta & -s_\theta \\ s_\theta & c_\theta \end{pmatrix}\begin{pmatrix} \eta_8 \\ \eta_0 \end{pmatrix}, \tag{7}$$

with $s_\theta = \sin\theta$, $c_\theta = \cos\theta$, and θ the mixing angle. The masses of the η and the η' and their mixing angle θ can be expressed in terms of the parameters in Eq. (6)

$$M_\eta^2 = \frac{M_0^2}{2} + M_K^2 - \frac{\sqrt{M_0^4 - \frac{4M_0^2\Delta^2}{3} + 4\Delta^4}}{2}, \tag{8}$$

$$M_{\eta'}^2 = \frac{M_0^2}{2} + M_K^2 + \frac{\sqrt{M_0^4 - \frac{4M_0^2\Delta^2}{3} + 4\Delta^4}}{2}, \tag{9}$$

$$\sin\theta = -\left(\sqrt{1 + \frac{\left(3M_0^2 - 2\Delta^2 + \sqrt{9M_0^4 - 12M_0^2\Delta^2 + 36\Delta^4}\right)^2}{32\Delta^4}}\right)^{-1}, \tag{10}$$

with $\Delta^2 = M_K^2 - M_\pi^2$. We mention that it is enough for us to consider the LO chiral Lagrangian for the pNGBs in Eq. (6). The LO square masses of the pion and the kaon are linearly dependent on the quark masses via

$$M_\pi^2 = 2B\hat{m}, \qquad M_K^2 = B(\hat{m} + m_s). \tag{11}$$

With the previous setup, it is straightforward to calculate the charmed mesons (D and D_s) and pNGBs (π, K, η, and η') scattering amplitudes, which can be categorized into seven different stes of quantum numbers characterized by strangeness (S) and isospin (I). The general expressions for the scattering amplitudes $D_1(p_1) + \phi_1(p_2) \to D_2(p_3) + \phi_2(p_4)$ with definite strangeness and isospin can be written as

$$V^{(S,I)}_{D_1\phi_1\to D_2\phi_2}(s,t,u)=\frac{1}{F^2}\Big[\frac{C_{LO}}{4}(s-u)-4C_0h_0+2C_1h_1$$

$$-2C_{24}H_{24}(s,t,u)+2C_{35}H_{35}(s,t,u)\Big],$$

$$(12)$$

where s,t,u are the standard Mandelstam variables, and $H_{24}(s,t,u)$ and $H_{35}(s,t,u)$ are

$$H_{24}(s,t,u)=2h_2p_2\cdot p_4$$
$$+h_4(p_1\cdot p_2p_3\cdot p_4+p_1\cdot p_4p_2\cdot p_3),\quad(13)$$

$$H_{35}(s,t,u)=h_3p_2\cdot p_4$$
$$+h_5(p_1\cdot p_2p_3\cdot p_4+p_1\cdot p_4p_2\cdot p_3).\quad(14)$$

The coefficients C_i can be found in Table I and some explicit expressions of C_i are relegated to the Appendix.

Notice that we have additional channels for the $(S,I)=(1,0)$ and $(0,1/2)$ cases compared to the previous $SU(3)$

calculations [4,12,13,19] and the scattering amplitudes involving the η meson are also different from those references. Nevertheless, if we set the mixing angle θ to zero and use the Gell-Mann-Okubo mass relation $M_\eta^2=(4M_K^2-M_\pi^2)/3$, we explicitly verify that our results in Table I confirm the expressions in Refs. [4,12]. While comparing with the formulas in Ref. [19], our results do not agree with the item at the intersection of the column labeled by C_1 and the row labeled by $D_s\eta\to D_s\eta$. We also find that there are global sign differences between ours and those in Ref. [13] for the $D\pi\to D\eta$ and $D\pi\to D_s\overline{K}$ amplitudes in the case with $(S,I)=(0,1/2)$.

To continue the discussion, we perform the partial wave projections of the full amplitudes in Eq. (12) and the projection formula with definite angular momentum J is given by

$$\mathcal{V}^{(S,I)}_{J,D_1\phi_1\to D_2\phi_2}(s)=\frac{1}{2}\int_{-1}^{+1}d\cos\varphi P_J(\cos\varphi)$$
$$\times V^{(S,I)}_{D_1\phi_1\to D_2\phi_2}(s,t(s,\cos\varphi)),\quad(15)$$

TABLE I. The coefficients in the scattering amplitudes $V^{(S,I)}_{D_1\phi_1\to D_2\phi_2}(s,t,u)$ in Eq. (12). The channels are labeled by strangeness (S) and isospin (I). For the coefficients not shown explicitly in this table, we give their expressions in the Appendix.

(S,I)	Channels	C_{LO}	C_0	C_1	C_{24}	C_{35}
$(-1,0)$	$D\bar{K}\to D\bar{K}$	-1	M_K^2	M_K^2	1	-1
$(-1,1)$	$D\bar{K}\to D\bar{K}$	1	M_K^2	$-M_K^2$	1	1
$(2,\frac{1}{2})$	$D_sK\to D_sK$	1	M_K^2	$-M_K^2$	1	1
$(0,\frac{3}{2})$	$D\pi\to D\pi$	1	M_π^2	$-M_\pi^2$	1	1
$(1,1)$	$D_s\pi\to D_s\pi$	0	M_π^2	0	1	0
	$DK\to DK$	0	M_K^2	0	1	0
	$DK\to D_s\pi$	1	0	$-(M_K^2+M_\pi^2)/2$	0	1
$(1,0)$	$DK\to DK$	-2	M_K^2	$-2M_K^2$	1	2
	$DK\to D_s\eta$	$-\sqrt{3}c_\theta$	0	$C_1^{1,0\,DK\to D_s\eta}$	0	$C_{35}^{1,0\,DK\to D_s\eta}$
	$D_s\eta\to D_s\eta$	0	$C_0^{1,0\,D_s\eta\to D_s\eta}$	$C_1^{1,0\,D_s\eta\to D_s\eta}$	1	$C_{35}^{1,0\,D_s\eta\to D_s\eta}$
	$DK\to D_s\eta'$	$-\sqrt{3}s_\theta$	0	$C_1^{1,0\,DK\eta\to D_s\eta'}$	0	$C_{35}^{1,0\,DK\eta\to D_s\eta'}$
	$D_s\eta\to D_s\eta'$	0	$C_0^{1,0\,D_s\eta\to D_s\eta'}$	$C_1^{1,0\,D_s\eta\to D_s\eta'}$	0	$C_{35}^{1,0\,D_s\eta\to D_s\eta'}$
	$D_s\eta'\to D_s\eta'$	0	$C_0^{1,0\,D_s\eta'\to D_s\eta'}$	$C_1^{1,0\,D_s\eta'\to D_s\eta'}$	1	$C_{35}^{1,0\,D_s\eta'\to D_s\eta'}$
$(0,\frac{1}{2})$	$D\pi\to D\pi$	-2	M_π^2	$-M_\pi^2$	1	1
	$D\eta\to D\eta$	0	$C_0^{0,\frac{1}{2}\,D\eta\to D\eta}$	$C_1^{0,\frac{1}{2}\,D\eta\to D\eta}$	1	$C_{35}^{0,\frac{1}{2}\,D\eta\to D\eta}$
	$D_s\bar{K}\to D_s\bar{K}$	-1	M_K^2	$-M_K^2$	1	1
	$D\eta\to D\pi$	0	0	$M_\pi^2(\sqrt{2}s_\theta-c_\theta)$	0	$c_\theta-\sqrt{2}s_\theta$
	$D_s\bar{K}\to D\pi$	$-\frac{\sqrt{6}}{2}$	0	$-\sqrt{6}(M_K^2+M_\pi^2)/4$	0	$\frac{\sqrt{6}}{2}$
	$D_s\bar{K}\to D\eta$	$-\frac{\sqrt{6}}{2}c_\theta$	0	$C_1^{0,\frac{1}{2}\,D_sK\to D\eta}$	0	$C_{35}^{0,\frac{1}{2}\,D_sK\to D\eta}$
	$D\eta'\to D\pi$	0	0	$-M_\pi^2(\sqrt{2}c_\theta+s_\theta)$	0	$s_\theta+\sqrt{2}c_\theta$
	$D\eta\to D\eta'$	0	$C_0^{0,\frac{1}{2}\,D\eta\to D\eta'}$	$C_1^{0,\frac{1}{2}\,D\eta\to D\eta'}$	0	$C_{35}^{0,\frac{1}{2}\,D\eta\to D\eta'}$
	$D_s\bar{K}\to D\eta'$	$-\frac{\sqrt{6}}{2}s_\theta$	0	$C_1^{0,\frac{1}{2}\,D_s\bar{K}\to D\eta'}$	0	$C_{35}^{0,\frac{1}{2}\,D_s\bar{K}\to D\eta'}$
	$D\eta'\to D\eta'$	0	$C_0^{0,\frac{1}{2}\,D\eta'\to D\eta'}$	$C_1^{0,\frac{1}{2}\,D\eta'\to D\eta'}$	1	$C_{35}^{0,\frac{1}{2}\,D\eta'\to D\eta'}$

where φ stands for the scattering angle between the incoming and outgoing particles in the center-of-mass frame, and the Mandelstam variable t is given by

$$
\begin{aligned}
t(s, \cos\varphi) = {} & M_{D_1}^2 + M_{D_2}^2 \\
& - \frac{1}{2s}(s + M_{D_1}^2 - M_{\phi_1}^2)(s + M_{D_2}^2 - M_{\phi_2}^2) \\
& - \frac{\cos\varphi}{2s}\sqrt{\lambda(s, M_{D_1}^2, M_{\phi_1}^2)\lambda(s, M_{D_2}^2, M_{\phi_2}^2)}.
\end{aligned}
\tag{16}
$$

with $\lambda(a,b,c) = a^2 + b^2 + c^2 - 2ab - 2bc - 2ac$ the Källén function. We will be only interested in the S-wave projection in this work, i.e., the $J = 0$ case. Therefore, the subscript J labeling different partial wave amplitudes $\mathcal{V}_{J,D_1\phi_1 \to D_2\phi_2}^{(S,I)}(s)$ will be dropped in later discussions for simplicity.

The perturbative scattering amplitudes at any finite order alone cannot generate resonances or bound states. Unitarity must be taken into account to study the resonances or bound states in the two-body scattering processes. We use the unitarization approach that has been extensively employed to discuss the $D_{s0}^*(2317)$ previously in Refs. [12,13,16,18,19]. This unitarization method was also used to study many other important phenomenons in hadron physics, such as the light-flavor meson resonances [27,28,38], the $\Lambda(1405)$ [39], etc. The unitarized two-body scattering amplitude in this formalism is given by [39]

$$
T(s) = [1 - \mathcal{V}(s) \cdot g(s)]^{-1} \cdot \mathcal{V}(s),
\tag{17}
$$

where $\mathcal{V}(s)$ stands for the partial wave amplitude in Eq. (15) and for simplicity the super–and subscripts have been dropped. The function $g(s)$ collects the unitarity cuts generated by the intermediate two-particle states in question. The loop function $g(s)$ is

$$
\begin{aligned}
g(s) = {} & i \int \frac{d^4 q}{(2\pi)^4} \frac{1}{(q^2 - M_D^2 + i\epsilon)[(P - q)^2 - M_\phi^2 + i\epsilon]}, \\
& s \equiv P^2,
\end{aligned}
\tag{18}
$$

which can be calculated in a once-subtracted dispersion relation or in dimensional regularization by replacing the divergence by a constant. The explicit form of $g(s)$ reads [38]

$$
\begin{aligned}
g(s) = {} & \frac{1}{16\pi^2}\left\{ a(\mu) + \ln\frac{M_D^2}{\mu^2} + \frac{s - M_D^2 + M_\phi^2}{2s}\ln\frac{M_\phi^2}{M_D^2} \right. \\
& + \frac{\sigma}{2s}[\ln(s - M_\phi^2 + M_D^2 + \sigma) - \ln(-s + M_\phi^2 - M_D^2 + \sigma) \\
& \left. + \ln(s + M_\phi^2 - M_D^2 + \sigma) - \ln(-s - M_\phi^2 + M_D^2 + \sigma)] \right\},
\end{aligned}
\tag{19}
$$

with $\sigma = \sqrt{\lambda(s, M_D^2, M_\phi^2)}$ and μ the regularization scale. The function $g(s)$ is independent of the scale μ and the explicit μ-dependence in Eq. (19) is compensated by the μ-dependent subtraction constant $a(\mu)$. To be specific, we set $\mu = 1$ GeV in the numerical discussions, in order to make a clear comparison with the previous works [12,21]. In this way, the value of the subtraction constant $a(\mu)$ determined in our fits correspond to its value at the scale 1 GeV.

The formalism for the unitarized partial-wave amplitude in Eq. (17) can be easily generalized to the coupled-channel case, where the quantities $\mathcal{V}(s)$ and $g(s)$ should be understood as matrices. The matrix elements for $\mathcal{V}(s)$ can be calculated using Eq. (15). Further, $g(s)$ in the coupled-channel case becomes a diagonal matrix, with its matrix elements given by Eq. (19) with the pertinent values for M_D and M_ϕ.

III. FITS TO LATTICE SIMULATION DATA

Up to now, there are no experimental measurements on the charmed meson and pNGB scattering. On the other hand, lattice QCD simulations are much advanced in this research field [4–7] and can provide us with valuable information to constrain the interactions between the charmed mesons and the pNGBs. The useful information that lattice simulations provides are the $D\phi$ scattering lengths. In the channel with definite strangeness and isospin, the S-wave scattering lengths are related to the unitarized scattering amplitudes $T(s)$ in Eq. (17) via

$$
\begin{aligned}
a_{D\phi \to D\phi}^{(S,I)} = {} & -\frac{1}{8\pi(M_D + M_\phi)}T_{J=0}^{(S,I)}(s_{\text{thr}})_{D\phi \to D\phi}, \\
& s_{\text{thr}} = (M_D + M_\phi)^2.
\end{aligned}
\tag{20}
$$

In order to make a comparison with the existing lattice-QCD data, the scattering lengths should be extrapolated to the unphysical quark masses via

$$
\begin{aligned}
M_K &= \sqrt{\mathring{M}_K^2 + \frac{1}{2}M_\pi^2}, \\
M_D &= \sqrt{\mathring{M}_D^2 + 2(2h_0 + h_1)M_\pi^2}, \\
M_{D_s} &= \sqrt{\mathring{M}_{D_s}^2 + 4h_0 M_\pi^2},
\end{aligned}
\tag{21}
$$

which are obtained from Eqs. (1), (4), and (6). Here, $\mathring{M}_K$, $\mathring{M}_D$, and $\mathring{M}_{D_s}$ denote the masses in the limit of $M_\pi^2(\propto \hat{m}) \to 0$, but with the strange quark mass $m_s \neq 0$ (the so-called two-flavor chiral limit). We mention that the quantities $\mathring{M}_K$, $\mathring{M}_D$, and $\mathring{M}_{D_s}$ do not represent their values in the (three-flavor) chiral limit, since they are still dependent on m_s. Their forms read

$$\overset{\circ}{M}{}^2_K = B m_s,$$

$$\overset{\circ}{M}{}^2_D = \overline{M}^2_D + 4 h_0 \overset{\circ}{M}{}^2_K,$$

$$\overset{\circ}{M}{}^2_{D_s} = \overline{M}^2_D + 4(h_0 + h_1) \overset{\circ}{M}{}^2_K, \qquad (22)$$

where $\overline{M}_D$ is the chiral limit mass of the charmed mesons, see Eq. (1). Combining Eqs. (11), (21) and (22), one can easily perform the chiral extrapolations by varying the light quark mass $\hat{m}$ and the strange quark mass m_s. The corresponding light-quark mass dependences for M_η, $M_{\eta'}$ and the mixing angle θ are obtained by combining Eqs. (11), (8), (9), and (10). Compared to the previous works in Refs. [12,18,19], we do not further make the expansion of M_π inside the square roots in the right-hand-sides of Eq. (21) in order to obtain M_K, M_D, and M_{D_s}. It is worthwhile to note that the present lattice simulations are performed with fixed strange- and charm-quark masses, while only the up/down-quark masses are varied. In addition, the fixed strange and charm masses are usually set at (slightly) unphysical values in lattice QCD simulations and, furthermore, different configurations may adopt different values, which finally lead to different values for $\overset{\circ}{M}_K$, $\overset{\circ}{M}_D$, and $\overset{\circ}{M}_{D_s}$. In our case, the lattice QCD data are taken from two collaborations, e.g. Ref. [4] and Refs. [5–7], and the values of $\overset{\circ}{M}_K$, $\overset{\circ}{M}_D$, and $\overset{\circ}{M}_{D_s}$ corresponding to different lattice configurations, as well as their values extracted from the physical case, are listed in Table II for easy comparison.

Next we present our fit procedure. The unknown parameters are $F, M_0, h_{i=0,1,2,3,4,5}$, and the subtraction constants a. Since we only work at leading order in the pNGB sector (6), it is justified to approximate the value of F by the physical pion decay constant $F_\pi = 92.2$ MeV. For M_0, we adopt the LO value $M_0 = 835.7$ MeV determined in Ref. [40], which has taken into account the recent lattice simulation data on the η and η' masses [41]. The LECs h_0 and h_1 are determined by the masses of the D and D_s mesons via Eq (21) and h_0 by the slopes of lattice QCD data for the masses of the D and the D_s while h_1 is fixed from the physical mass splitting between D and D_s. The resulting numerical values can be found in the first two rows in Table III.

Further, redefinitions of the remaining LECs, i.e., $h_{i=2,3,4,5}$, are introduced in order to reduce the correlations

TABLE II. The masses defined in the limit $M_\pi \to 0$ in Eq. (22) for the chiral extrapolations.

		Ensemble (1)	Ensemble (2)	
	Ref. [4]	[5–7]	[5–7]	Physical
$\overset{\circ}{M}_K$ [MeV]	560.8	519.0	482.8	486.3
$\overset{\circ}{M}_D$ [MeV]	1940	1538	1631	1862
$\overset{\circ}{M}_{D_s}$ [MeV]	2058	1655	1731	1967

TABLE III. Fitting results of the parameters. The fitting results labeled by Table V are taken from Ref. [4] for comparison. Fit-6C and Fit-5C denote six- and five-channel fits, respectively. h_0 and h_1 are determined by the masses of the D and the D_s, not by the scattering lengths. See the text for details.

LEC	Fit-6C	Fit-5C	Table V [4]
h_0	0.033*	0.033*	0.014*
h_1	0.43*	0.43*	0.42*
h_{24}	$-0.13^{+0.05}_{-0.06}$	$-0.13^{+0.05}_{-0.06}$	$-0.10^{+0.05}_{-0.06}$
h_{35}	$0.23^{+0.06}_{-0.06}$	$0.24^{+0.12}_{-0.12}$	$0.25^{+0.13}_{-0.13}$
h'_4	$-0.21^{+0.29}_{-0.27}$	$-0.19^{+0.32}_{-0.31}$	$-0.32^{+0.35}_{-0.34}$
h'_5	$-1.78^{+0.19}_{-0.19}$	$-1.83^{+0.57}_{-0.56}$	$-1.88^{+0.63}_{-0.61}$
a ($\lambda = 1$ GeV)	$-1.88^{+0.06}_{-0.06}$	$-1.88^{+0.07}_{-0.09}$	$-1.88^{+0.07}_{-0.09}$
χ^2/d.o.f.	$\frac{12.27}{16-5} \cong 1.12$	$\frac{12.26}{15-5} \cong 1.23$	1.06

during the fitting process, as done in Refs. [4,21]. These take the form

$$h_{24} \equiv h_2 + h'_4, \qquad h_{35} \equiv h_3 + 2h'_5,$$

$$h'_4 \equiv h_4 \hat{M}^2_D, \qquad h'_5 \equiv h_5 \hat{M}^2_D, \qquad (23)$$

with $\hat{M}_D \equiv (M^{\text{phys}}_D + M^{\text{phys}}_{D_s})/2$ the averaged physical masses of D and D_s. The redefined LECs are dimensionless and used as fitting variables. A common subtraction constant a, occurring in the loop function in Eq. (19), is adopted for all the possible channels.[1] Then the redefined LECs h_i in Eq. (23) and the subtraction constant a are fitted to the lattice scattering lengths provided in Refs. [4–7]. We stress that our fits are done using directly the lattice QCD data for the various masses, rather than those derived from Eq. (21) together with the masses shown in Table II. We mention that our treatment of the masses in the fits is the same as that in Ref. [13], but different from the one in Ref. [12], which used the masses resulting from the chiral extrapolations in Eq. (21). For reference, the correlation coefficients between the fit parameters for Fit-6C, explained later, from CERN MINUIT minimization package are shown in Table IV. It is worth noting that the correlations of the different lattice simulation data are not considered in our fits and hence the correlations of the fit parameters might be underestimated.

Most of the data from the present lattice simulations are for the single-channel cases, e.g., $(S, I) = (-1, 0), (-1, 1), (2, 1/2), (0, 3/2)$ and the $D_s \pi$ channel in the $(S, I) = (1, 1)$ case [4]. The lattice simulations for the $(S, I) = (1, 0)$ case, where the $D^*_{s0}(2317)$ appears, are still quite limited. Only

---

[1]In general, the subtraction constant $a(\mu)$ should be channel dependent. However, if distinct subtraction constants are adopted in different channels, our fits tend to be unstable. This indicates that the present lattice simulation data are still not precise enough to discriminate the individual subtraction constants in different channels.

TABLE IV. The correlation coefficients between different parameters result from the MINUIT program.

	Global	h_{24}	h_{35}	h'_4	h'_5	a
h_{24}	0.983	1.000	−0.493	−0.697	0.135	0.677
h_{35}	0.889	−0.493	1.000	−0.165	−0.546	−0.761
h'_4	0.971	−0.697	−0.165	1.000	0.501	−0.001
h'_5	0.954	0.135	−0.546	0.501	1.000	0.780
a	0.981	0.677	−0.761	−0.001	0.780	1.000

two data points are given in Refs. [5–7]: one is determined with a $N_f = 2$ simulation and the other is obtained with $N_f = 2 + 1$. To evaluate the effect of these two data points from the $(S, I) = (1, 0)$ simulations in the fit, we perform two different types of fits. The first one is a five-channel fit, denoted as Fit-5C for short, where the data for the coupled $DK(I = 0)$ channel are not included in the fit, e.g., only the data points in the $(S, I) = (−1, 0), (−1, 1), (2, 1/2),$ $(0, 3/2), (1, 1)$ cases from Ref. [4] are considered. Compared to the five-channel fit shown in Table V from Ref. [4], the coupled-channel effect for $D_s\pi$ is included here. To be more specific, we include the lattice QCD data corresponding to pion masses, 301, 364 and 511 MeV from Ref. [4] in the Fit-5C case. The points for $M_\pi > 600$ MeV are excluded in the fits, since such a large value may

challenge a reliable chiral extrapolation. The fit results for the parameters are given in the column labeled as Fit-5C in Table III and the reproduction of the lattice simulation data can be seen in Fig. 1. In the last panel of this figure, we make a prediction for the DK scattering length in the $(S, I) = (1, 0)$ case, where in order to make a clear comparison of the lattice data from Ref. [7] we have used the masses of the D and D_s from that reference to make the plots, e.g., the results in the Ensemble (2) column in Table II. Notice that we do not explicitly show the error bands of the predictions in the last panel of Fig. 1, since the error bands are so huge that they almost cover the whole region of that panel. It is quite clear that our central predictions prefer the $N_f = 2 + 1$ simulation result over the $N_f = 2$ one. This inspires us to perform another type of fit, where we explicitly include the $N_f = 2 + 1$ datum from Refs. [6,7] in the fit. This fit will be named as Fit-6C in later discussions, as in this case we have six channels in the fit. The fit results of the LECs and the subtraction constant are compiled in the column labeled as Fit-6C in Table III and the comparisons between our chiral extrapolations using Eq. (21) and lattice QCD data are displayed in Fig. 2. Due to the inclusion of the coupled channel effects, improvements are achieved in the sense that the error bars become smaller, especially for the results in Fit-6C. Nevertheless, our results and those in Ref. [4] are compatible within the
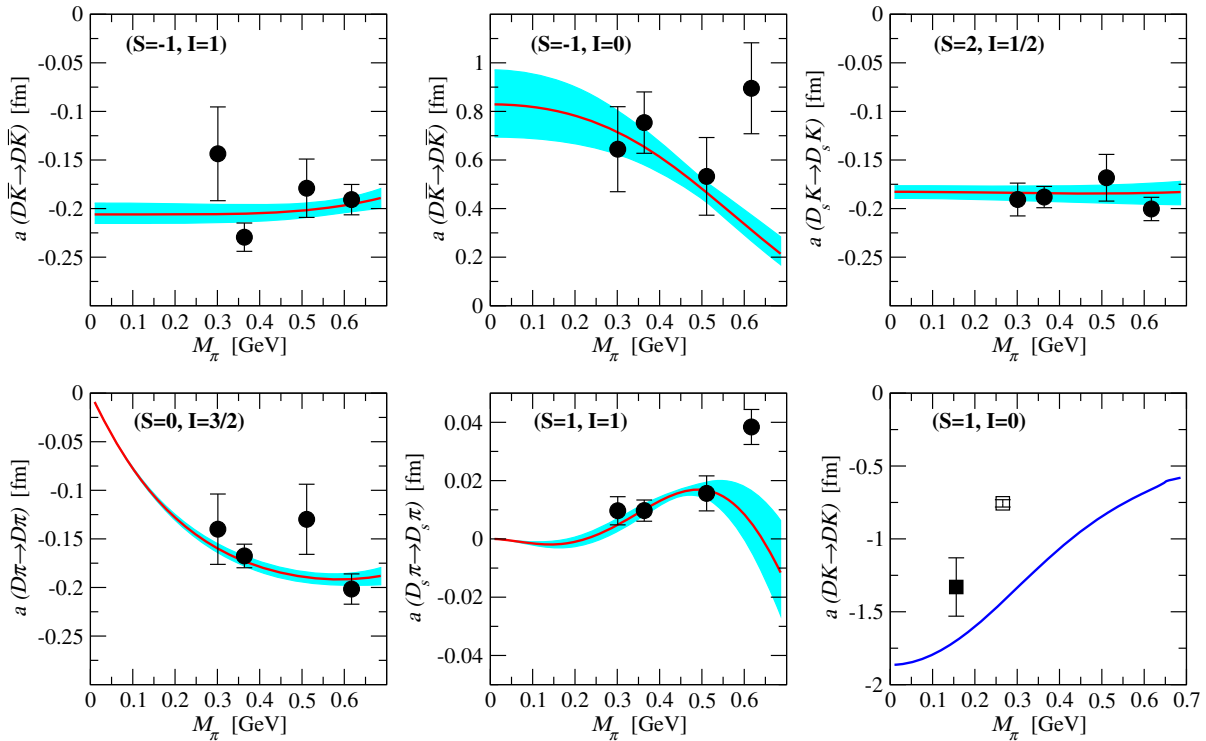

FIG. 1 (color online). 5-channel Fit (Fit-5C). The bands represent the variation of the scattering lengths with the LECs varying within 1-σ uncertainty. The black solid circles with error bars stand for the lattice QCD data from Ref. [4]. The open and solid squares with error bars denote the $N_f = 2$ and $N_f = 2 + 1$ lattice QCD data from Ref. [6], respectively. The blue solid line in the $(S = 1, I = 0)$ panel is our prediction, see the text for details.
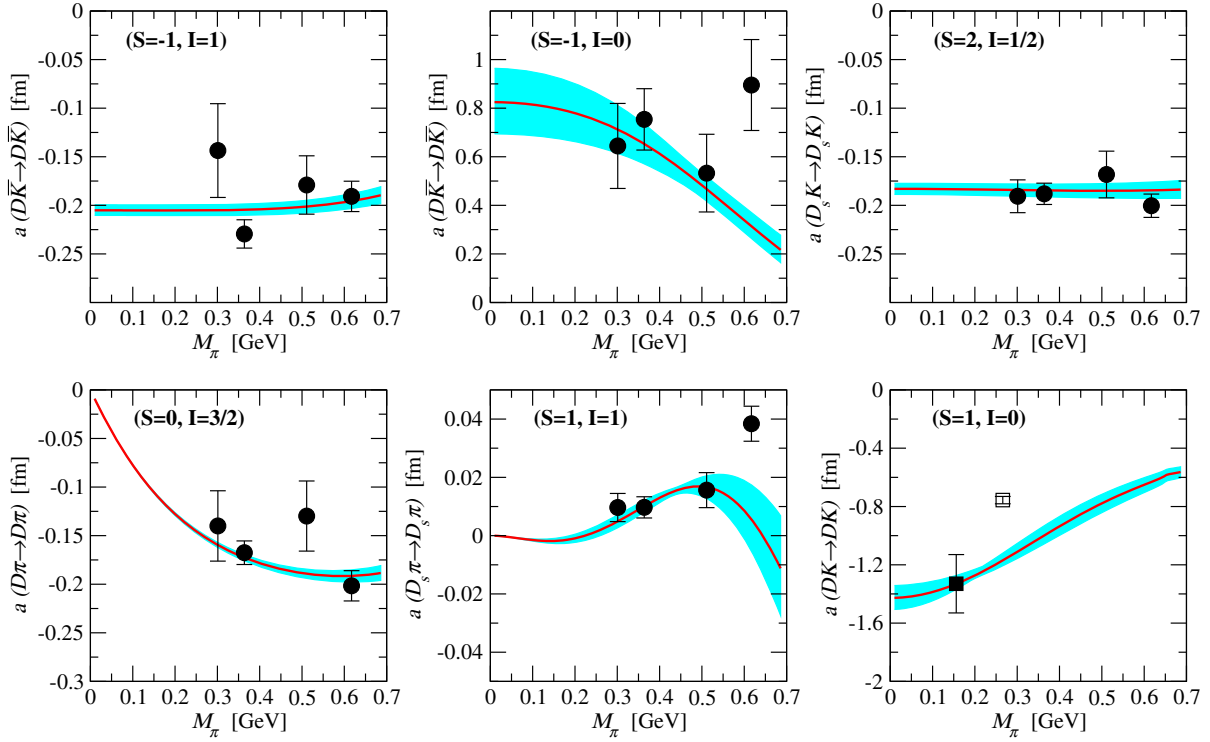
FIG. 2 (color online).   6-channel fit (Fit-6C). The bands represent the variation of the scattering lengths with the LECs varying within 1-σ uncertainty. See Fig. 1 for further details.

uncertainties and the resulting values for LECs are quite similar, see Table III for comparisons. The corresponding descriptions of the lattice QCD data are all of good quality with a χ^2 per d.o.f around 1.0, which can also be seen from the plots in Fig. 1 and Fig. 2. In Figs. 1 and 2, the shaded bands represent the variation of the scattering lengths with the LECs whose values vary within a 1-σ uncertainty.

Our prediction for the chiral extrapolation of $D\pi$ scattering length with $(S, I) = (0, 1/2)$ is given in Fig. 3, where we have used the masses in the column labeled by "Physical" in Table II. In addition, with the LECs obtained in Table III and masses specified at their corresponding physical values, we predict all the physical S-wave scattering lengths in Table V.
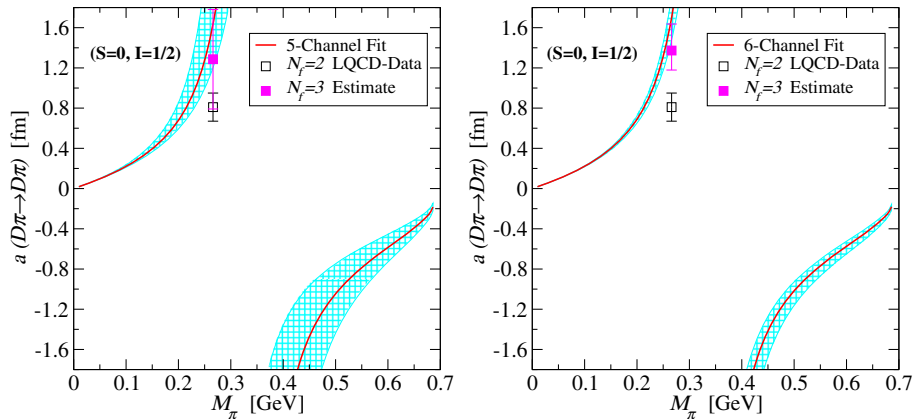
FIG. 3 (color online).   Predictions for the $D\pi \to D\pi$ scattering lengths in the $(S = 0, I = 1/2)$ channel. The red lines with the cyan grid bands represent the chiral extrapolations of the scattering lengths with the masses specified by the last column in Table II and the LECs varying within their 1-σ uncertainties shown in Table III. The open black square with error bar denotes the $N_f = 2$ lattice QCD data taken from Ref. [5]. The magenta solid square with error bar is our estimate based on the masses of Ensemble (2) in Table II and LECs in Table III.

TABLE V.   Predictions of the scattering lengths using the parameters from Table III together with the physical masses for the charmed and light pseudoscalar mesons.

(S, I)	Channels	Fit-5C	Fit-6C
$(-1, 0)$	$D\bar{K} \to D\bar{K}$	$1.27^{+0.49}_{-0.36}$	$1.26^{+0.46}_{-0.32}$
$(-1, 1)$	$D\bar{K} \to D\bar{K}$	$-0.21^{+0.02}_{-0.01}$	$-0.21^{+0.01}_{-0.01}$
$(2, \frac{1}{2})$	$D_s K \to D_s K$	$-0.19^{+0.01}_{-0.01}$	$-0.19^{+0.01}_{-0.01}$
$(0, \frac{3}{2})$	$D\pi \to D\pi$	$-0.101^{+0.003}_{-0.003}$	$-0.101^{+0.001}_{-0.001}$
$(1, 1)$	$D_s\pi \to D_s\pi$	$0.004^{+0.001}_{-0.001}$	$0.004^{+0.001}_{-0.001}$
	$DK \to DK$	$0.06^{+0.03}_{-0.03} + i0.17^{+0.02}_{-0.01}$	$0.06^{+0.03}_{-0.03} + i0.17^{+0.01}_{-0.01}$
$(1, 0)$	$DK \to DK$	$-0.92^{+0.22}_{-0.40}$	$-0.89^{+0.06}_{-0.10}$
	$D_s\eta \to D_s\eta$	$-0.27^{+0.01}_{-0.01} + i0.03^{+0.01}_{-0.01}$	$-0.27^{+0.01}_{-0.01} + i0.03^{+0.01}_{-0.01}$
	$D_s\eta' \to D_s\eta'$	$-0.22^{+0.03}_{-0.01} + i0.01^{+0.01}_{-0.01}$	$-0.22^{+0.01}_{-0.01} + i0.01^{+0.01}_{-0.01}$
$(0, \frac{1}{2})$	$D\pi \to D\pi$	$0.35^{+0.04}_{-0.02}$	$0.35^{+0.01}_{-0.01}$
	$D\eta \to D\eta$	$0.02^{+0.06}_{-0.04} + i0.03^{+0.03}_{-0.01}$	$0.02^{+0.02}_{-0.02} + i0.03^{+0.01}_{-0.01}$
	$D_s\bar{K} \to D_s\bar{K}$	$-0.05^{+0.04}_{-0.06} + i0.35^{+0.07}_{-0.03}$	$-0.05^{+0.02}_{-0.02} + i0.35^{+0.04}_{-0.03}$
	$D\eta' \to D\eta'$	$0.16^{+0.64}_{-0.22} + i0.05^{+0.26}_{-0.03}$	$0.34^{+0.31}_{-0.14} + i0.04^{+0.12}_{-0.02}$

IV. POLE ANALYSES ON THE CHARM SCALAR STATES

A. Pole contents in the physical situation

Experimentally observed bound states and resonances correspond to the poles of the partial-wave amplitudes in physical and unphysical Riemann sheets (RS), respectively. In this section, we utilize the previously determined LECs and subtraction constant to study the pole contents in the charmed mesons and pNGBs scattering amplitudes. In our formalism, different Riemann sheets are characterized by the sign of the imaginary part of the loop function $g(s)$ in Eq. (19). Each $g(s)$ is associated with two sheets. By default the expression in Eq. (19) defines the first/physical Riemann sheet. To reverse the sign of the imaginary part of the $g(s)$ function in Eq. (19), one then analytically extrapolates to the unphysical Riemann sheet. For scattering processes in question, different Riemann sheets can be accessed by choosing the proper signs of the imaginary parts of the $g_i(s)$ functions, with $g_i(s)$ calculated from the two intermediate states in the ith-channel. The first Riemann sheet will be labeled as $(+, +, +, …)$. The second and third sheets can be accessed by reversing the signs of the imaginary parts of the $g(s)$ functions defined at the first and second thresholds, which will be denoted by $(-, +, +, …)$ and $(-, -, +, …)$, in order. Besides the pole positions, the residues for a given pole calculated in the partial-wave amplitudes in different channels can also provide useful information, since the residues correspond to the coupling strengths between the pole and its interacting $D\phi$ modes.

Since the results in Table III for Fit-5C and Fit-6C are quite similar, we only present the pole analyses for the Fit-6C case in the following. Nevertheless, we stress that we

have explicitly verified that the poles and their residues from the two fit results look indeed very similar. The pole positions and their residues in different channels, which are calculated by using the physical masses for the charmed mesons and pNGBs, are summarized in Table VI. Some remarks about the comparisons of our results for the charm scalar meson spectra with the previous ones in literature and experimental measurements are in order.

A virtual-state pole at around 2.3 GeV is found in the single channel with $(S, I) = (-1, 0)$. In the $(S, I) = (0, 3/2)$ channel a very broad resonance with the width around 500 MeV is obtained. Such a broad resonance is difficult to be verified in experiments.

For the $(S, I) = (1, 1)$ case with two coupled channels, we find one broad 2nd-Riemann-sheet pole above the DK threshold and one broad 3rd-Riemann-sheet pole below the DK threshold. The former one is mainly coupled to DK and the latter is coupled more or less equally to both $D_s\pi$ and DK. Our results are different from those in Ref. [19], especially that our width for the 2nd-Riemann-sheet pole is much larger than that in the previous reference. These differences are presumably caused by the fact that the results in Ref. [19] are obtained replying on the preliminary scattering length data from Ref. [42], which somewhat differ from the final published data that we used in this work, given in Ref. [4]. It is quite interesting to point out that an enhancement in the $D^0 K^+$ invariant mass around 2350–2500 MeV was very recently observed [43], which may be an evidence of the existence of the pole with $\sqrt{s_{\text{pole}}} = 2466^{+32}_{-27} - i271^{+4}_{-5}$ in Table VI.

In the $(S, I) = (1, 0)$ case, a bound-state pole at 2321^{+6}_{-3} is found and it corresponds to the physical $D_{s0}^*(2317)$ state. We further verify that the $D_{s0}^*(2317)$ is most strongly coupled to the DK system, as can be seen by its residues in

TABLE VI.   Poles and their residues based on Fit-6C in Table III. Physical masses for the charmed and light pseudoscalar mesons are used to obtain the results in this table. The Riemann sheets on which the poles are located are indicated in the second column. In the last column, we give the ratios of the residues with respect to the first threshold.

(S, I)	RS	$\sqrt{s_{\text{pole}}}$ [MeV]	$|\text{Residue}|^{1/2}$ [GeV]	Ratios	
$(-1, 0)$	II	2333^{+15}_{-36}	$7.45^{+3.56}_{-1.38}(D\bar{K})$		
$(0, \frac{3}{2})$	II	$2033^{+3}_{-3} - i251^{+3}_{-3}$	$6.64^{+0.04}_{-0.04}(D\pi)$		
$(1, 1)$	II	$2466^{+32}_{-27} - i271^{+4}_{-5}$	$6.95^{+0.60}_{-0.37}(D_s\pi)$	$1.72^{+0.12}_{-0.15}(DK/D_s\pi)$	
	III	$2225^{+12}_{-9} - i178^{+19}_{-17}$	$7.35^{+0.19}_{-0.13}(D_s\pi)$	$0.80^{+0.04}_{-0.04}(DK/D_s\pi)$	
$(1, 0)$	I	2321^{+6}_{-3}	$9.30^{+0.04}_{-0.12}(DK)$	$0.77^{+0.02}_{-0.02}(D_s\eta/DK)$	$0.43^{+0.15}_{-0.13}(D_s\eta'/DK)$
	II	2356^{+1}_{-1}	$2.85^{+0.08}_{-0.13}(DK)$	$0.69^{+0.01}_{-0.01}(D_s\eta/DK)$	$0.38^{+0.12}_{-0.11}(D_s\eta'/DK)$
$(0, \frac{1}{2})$	II	$2114^{+3}_{-3} - i111^{+8}_{-7}$	$9.66^{+0.15}_{-0.13}(D\pi)$	$0.31^{+0.03}_{-0.03}(D\eta/D\pi)$	$0.46^{+0.02}_{-0.02}(D_s\bar{K}/D\pi)$
				$0.49^{+0.08}_{-0.08}(D\eta'/D\pi)$	
	III	$2473^{+29}_{-22} - i140^{+8}_{-7}$	$5.36^{+0.40}_{-0.28}(D\pi)$	$1.09^{+0.06}_{-0.05}(D\eta/D\pi)$	$2.12^{+0.06}_{-0.08}(D_s\bar{K}/D\pi)$
				$1.12^{+0.18}_{-0.16}(D\eta'/D\pi)$	

Table VI. In addition, we also find a virtual-state pole just below the DK threshold on the second Riemann sheet. It is interesting to stress that the virtual pole is even closer to the DK threshold than the bound $D^*_{s0}(2317)$ state.

In the $(S, I) = (0, 1/2)$ channel, there are two poles: $\sqrt{s_{\text{pole}}} = 2114^{+3}_{-3} - i111^{+8}_{-7}$ and $\sqrt{s_{\text{pole}}} = 2473^{+29}_{-22} - i140^{+8}_{-7}$, located on the second and third Riemann sheets, respectively. The second-Riemann-sheet pole is consistent with the observations made in by Refs. [14–16,19]. This pole can be regarded as a broad $D^*_0(0, \frac{1}{2})$ state strongly coupled

to the $D\pi$ threshold. On the other hand, the third-Riemann-sheet pole, which is most strongly coupled to $D_s\bar{K}$, has a much broader width compared to the previous results [14,15,19] and our determination of its mass and width is close to those of $D^*_0(2460)$ announced by PDG [44].

B. Pole trajectories with varying pion mass

Due to the limited experimental measurements of the charm scalar mesons, lattice simulations provide a possible way to verify the poles from our analyses. Therefore it is
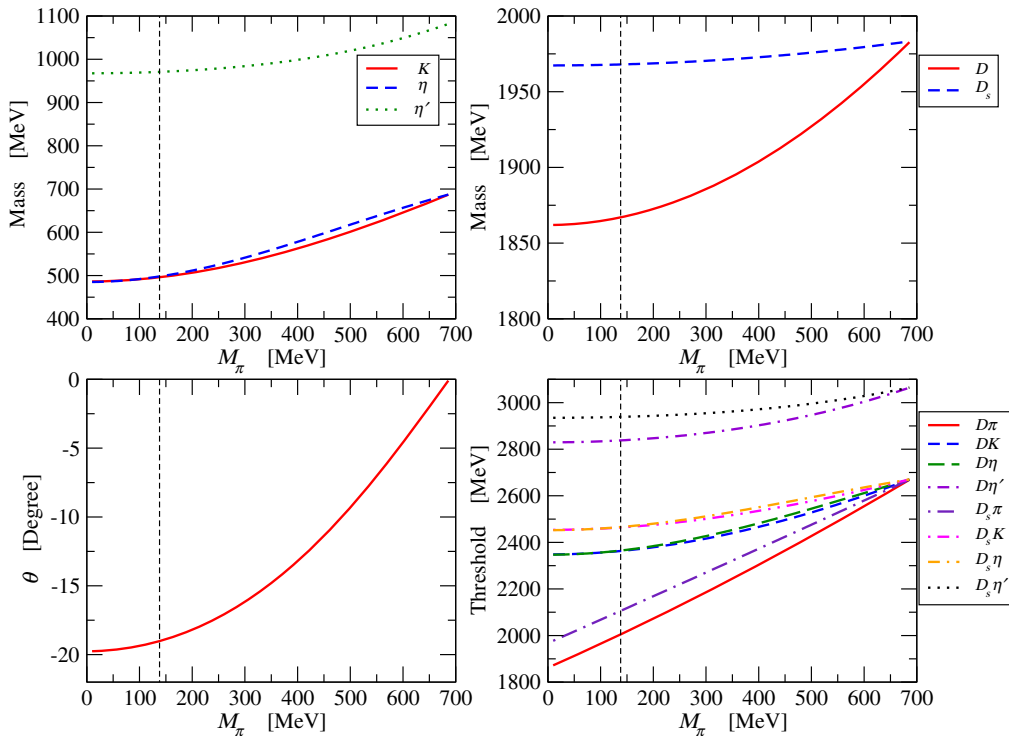

FIG. 4 (color online).   Masses for the pseudo-Goldstones bosons and the charmed D mesons, the LO $\eta - \eta'$ mixing angle and the thresholds as functions of M_π.
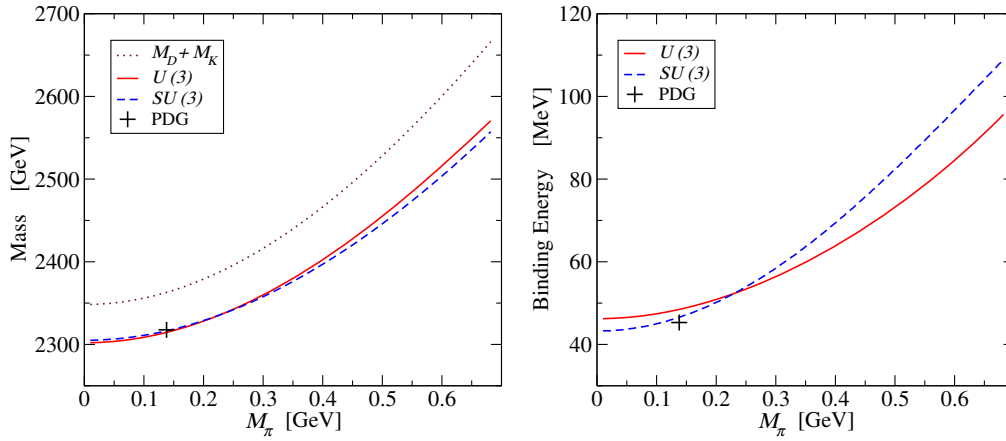
FIG. 5 (color online).   Properties of $D_{s0}(2317)$ pole masses when varying M_π: $U(3)$ v.s. $SU(3)$.

interesting to further probe the pole trajectories with varying pion mass M_π, which can be useful for comparisons with future lattice results. From the theoretical point of view, the M_π trajectories of the various poles can offer us further insights into the properties of different hadron states, as discussed, e.g., in Ref. [23]. Before investigating the M_π trajectories of the various poles, we first show how the masses of the K, η, η', D, D_s, their thresholds and the mixing angle θ change with varying pion mass in Fig. 4. We point out that in the discussions below we have used the physical strange quark mass, i.e., the values in the last column in Table II. All of the masses considered here are increased when enlarging the pion masses, and the mixing angle θ tends to increase as well. Around $M_\pi \sim 700$ MeV, it is clear from Fig. 4 that the masses of D and D_s become equal and the mixing angel θ approaches zero. This phenomenon is not a surprise, since when $M_\pi \simeq 690$ MeV, the pion and kaon masses turn out to be degenerate, indicating the exact $SU(3)$-flavor symmetry in that region.

The M_π trajectories for the $D_{s0}^*(2317)$ meson can be seen in Fig. 5. In the left panel, together with the varying thresholds $M_D + M_K$, we give the results for the pole positions of $D_{s0}^*(2317)$ on the first Riemann sheet, which are identified as its masses. In the right panel, we show the binding energies which are the gaps between the thresholds and the pole positions. The red solid lines in Fig. 5 stand for our final results of the $U(3)$ chiral theory with realistic descriptions of η and η', while the blue dashed lines labeled as $SU(3)$ are calculated by approximating our final expressions to mimic the $SU(3)$ case, which are obtained by setting $M_0 \to \infty$.[2] In this limit, the heavy singlet η_0 and the octet η_8 will be decoupled, and one can identify the octet η_8 as the physical η, as done in $SU(3)$ χPT [35]. In addition, when $M_0 \to \infty$ the effects from the channels with the heavy singlet η_0 will be much suppressed due to their far distance form the thresholds. The small variances

between the $U(3)$ and $SU(3)$ lines in Fig. 5 indicate that the final results for $D_{s0}^*(2317)$ are not very sensitive to the treatment of the η and the η' at least for low pion masses. This also explicitly justifies the previous study of $D_{s0}^*(2317)$ in Refs. [12–16,18,19] based on the $SU(3)$ treatment of η.

The most important conclusion obtained from Fig. 5 is that the $D_{s0}^*(2317)$ always stays a bound state below the DK threshold for a wide range of M_π. In contrast, the M_π trajectories of the pole around 2.1 GeV on the second Riemann sheet with $(S, I) = (0, 1/2)$ in Table VI are found to be quite complicated, as shown in Fig. 6. By increasing the value of M_π, we first see that both the real and imaginary parts of this pole tend to decrease on the second Riemann sheet. At some point around $M_\pi \sim 2M_\pi^{\text{phys}}$, the real part of this pole becomes lower than the threshold of $D\pi$, but its imaginary part is still nonzero. When M_π equals to 288 MeV, the pair of resonance poles meets at the point below the $D\pi$ threshold on the real axis and becomes two virtual states on the second Riemann sheet. If we further increase the value of the pion mass, one of the virtual poles goes further away from the threshold toward to the left side on the real axis, while the other one moves closer to the threshold on the right side and it becomes a bound state on the first Riemann sheet when $M_\pi > 336$ MeV. If we keep increasing the value of M_π, both the virtual and the bound state move further away from the threshold to the left side. It is very interesting to point out that the behavior for the broad charm scalar pole around 2.1 GeV with $(S, I) = (0, 1/2)$ looks quite similar to the one of the σ resonance $f_0(500)$ discussed in Refs. [22,23].

The pole trajectories with varying M_π for the charm scalar pole around 2.4 GeV in the third Riemann sheet with $(S, I) = (0, 1/2)$ are shown in Fig. 7. Compared to the trajectories in Fig. 6, the dependences of the pole around 2.4 GeV with M_π are much weaker and only mild changes of the pole positions are observed over a wide range of pion masses from 100 to 700 MeV.

___
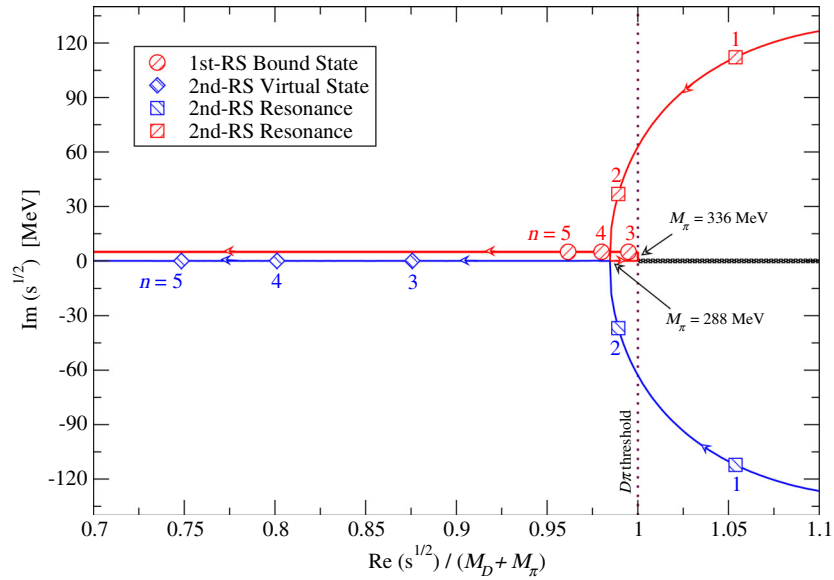[2]Strictly speaking, one would have to readjust the LECs, too.

FIG. 6 (color online). Trajectories of the $(S = 0, I = 1/2)$ resonance at around 2.1 GeV with varying M_π. n is defined by $M_\pi = n M_\pi^{\text{phys}}$.
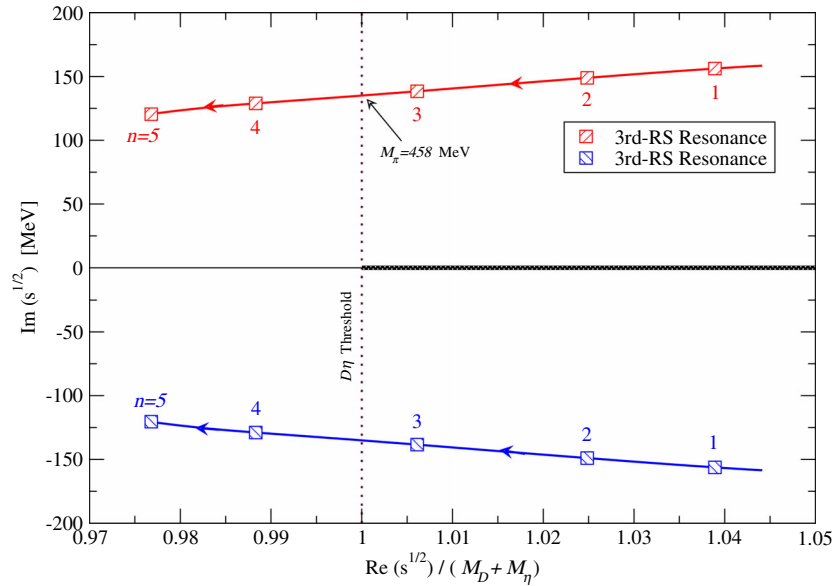

FIG. 7 (color online). Trajectories of the $(S = 0, I = 1/2)$ resonance at around 2.4 GeV with varying M_π. n is defined by $M_\pi = n M_\pi^{\text{phys}}$.

C. N_C trajectories for the charm scalar mesons

The N_C trajectory of a resonance/bound-state pole can provide us useful information about the inner structure of the particle. Extensive studies on the N_C trajectories for light-flavor resonances, such as $f_0(500)$, $f_0(980)$, $\rho(770)$, $a_1(1260)$, etc, have been carried out in literature [24–28,45,46]. As discussions on the N_C properties of the heavy-light mesons are still rare, one of the key goals of this work is to fill this gap. We point out that in order to make a

reliable study of the N_C trajectories for a given state, not only the N_C scaling of the couplings of the scattering amplitudes, but also the N_C running of the masses of the intermediate particles involved in the scattering, need to be carefully considered. As mentioned in the Introduction, the singlet η_0, with its large mass due to the QCD $U(1)_A$ anomaly effect, should be properly taken into account when discussing the N_C dependences, as the $U(1)_A$ anomaly is $1/N_C$ suppressed when $N_C \to \infty$ and η_0
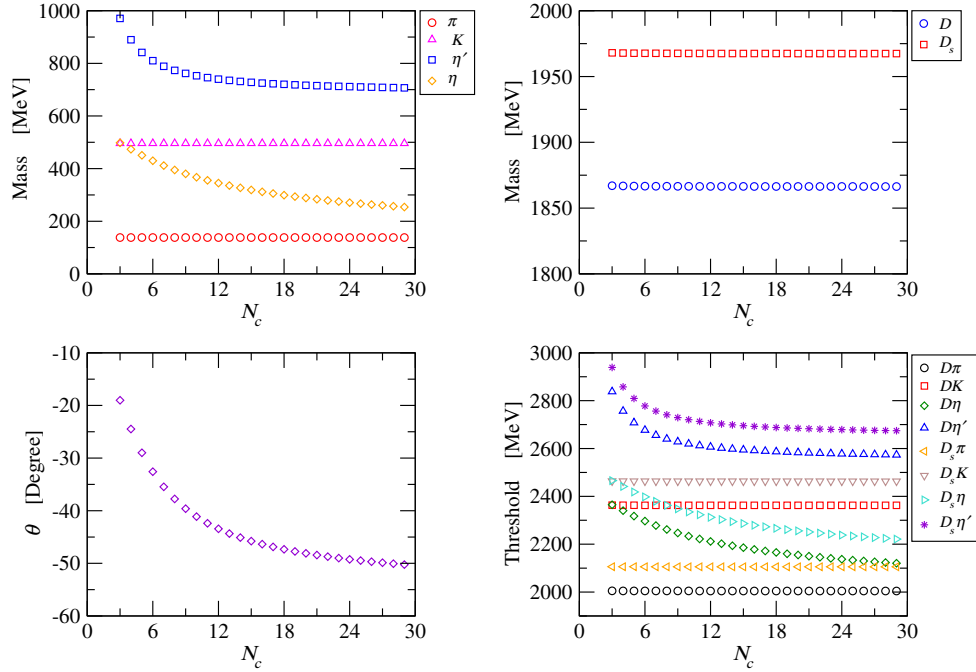
FIG. 8 (color online).   Masses for the pNGBs and charmed D mesons, the LO $\eta - \eta'$ mixing angle and the relevant thresholds as functions of N_C from 3 to 30 in steps of one unit.

then becomes the ninth pNGB in the chiral and large N_C limits.

For the N_C behaviors of the LECs in Eq. (4), their leading-order N_C scaling can be obtained by counting the number of traces in the corresponding operators. We take h_0 and h_1 as examples to illustrate this. The operator accompanied by h_1 has the same number of traces as the mass operator in Eq. (1), therefore h_1 has the same N_C scaling as the bare mass squared $\overline{M}_D^2$. The leading scaling of h_0 is one more power of $1/N_C$ suppressed since there is one additional trace in this operator. From the large N_C point of view, the mass of any $\overline{q}q$ meson behaves as a constant [47,48] and, therefore, the leading N_C scaling for $\overline{M}_D$, M_π, and M_K is $\mathcal{O}(1)$. As a result, the leading N_C scaling of h_1 is also $\mathcal{O}(1)$, while h_0 should be counted as $\mathcal{O}(1/N_C)$. Similar rules can be applied to other operators in Eq. (4) and we summarize their leading N_C scaling as follows

$$h_1, h_3, h_5 \sim \mathcal{O}(1), \qquad h_0, h_2, h_4 \sim \mathcal{O}(1/N_C). \quad (24)$$

The N_C scaling of the pNGB decay constant F in the chiral limit is $\mathcal{O}(\sqrt{N_C})$ [34,35] and the singlet η_0 mass squared M_0^2 is counted as $\mathcal{O}(1/N_C)$ [31–34]. For the subtraction constant a in Eq. (19), a reasonable assignment for its leading N_C scaling is $\mathcal{O}(1)$ as argued in Ref. [28] and we will also use this. With these assignments of the N_C scaling for different parameters, we can calculate the N_C running for other quantities.

In Fig. 8, we show the N_C scaling of the masses of the pNGBs and charmed D mesons, the $\eta - \eta'$ mixing angle and the relevant thresholds. A striking phenomenon from the first panel in Fig. 8 is that the η mass significantly decreases when N_C is increased and it tends to be equal to the pion mass in the large N_C limit. Contrary to this, when increasing the values of N_C, the mass of the η' decreases from the beginning, but it still has a relatively large mass around 700 MeV in the large N_C limit. These behaviors can be analytically understood from the leading order mixing formulas in Eqs. (8), (9), and (10). In the large N_C limit, one has $M_0 \to 0$ and in this limit one can easily obtain from Eqs. (8), (9), and (10) that

$$M_\eta = M_\pi, \quad M_{\eta'} = \sqrt{2M_K^2 - M_\pi^2}, \quad \arcsin\theta = -\sqrt{\frac{2}{3}}, \quad (25)$$

which perfectly explains the results in the two panels on the left side of Fig. 8. The results are consistent with the findings in Ref. [49]. The masses of the charmed $D_{(s)}$ mesons depend on the two LECs h_0 and h_1, as explicitly given in Eqs. (21) and (22). The final results for the N_C running of M_D and M_{D_s} are given in the top right panel in Fig. 8, which basically behave like constants when varying N_C. As a result, the N_C running of the thresholds as given in the bottom right panel is mainly caused by the running of M_η and $M_{\eta'}$. An important finding is that the order of the thresholds $M_{D_s} + M_\eta$ and $M_D + M_K$ is reversed and the former becomes lower than the latter for $N_C > 7$.
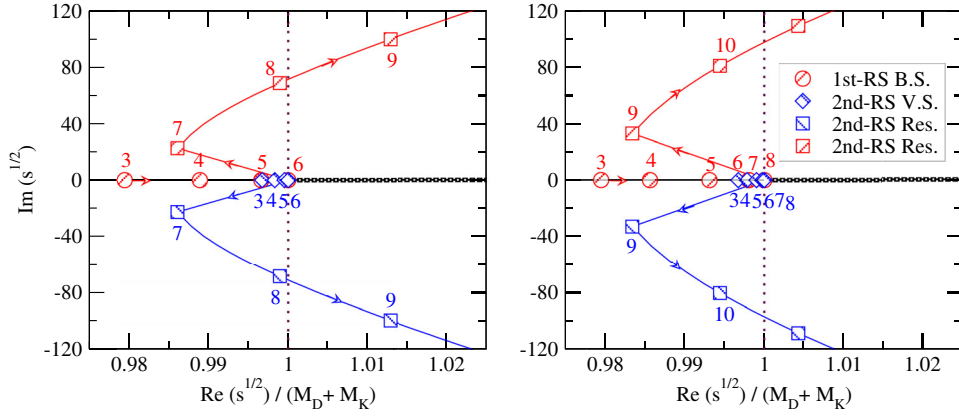
FIG. 9 (color online). N_C trajectories of the $D_{s0}^*(2317)$ pole. The numbers in the plots indicate the values of N_C. Left: results with leading N_C scaling laws in Eq. (24); Right: results by including the subleading N_C scaling effects in Eqs. (26) and (27).

The pole trajectories of the $D_{s0}^*(2317)$ with varying N_C are given in the left panel of Fig. 9 for the leading N_C scaling of h_i. In order to highlight the relative position of the pole and the DK threshold, we have normalized the units of the real axis in terms of $M_D + M_K$. The physical $D_{s0}^*(2317)$ state is represented by the bound-state pole at $N_C = 3$ on the first Riemann sheet, i.e., the left most point in the real axis in Fig. 9. We also find a virtual-state pole below the DK threshold on the real axis on the second Riemann sheet at $N_C = 3$, which is even closer to the threshold than the bound-state pole. The explicit values of the pole positions at $N_C = 3$ can be seen in Table VI. When increasing the values of N_C, we observe that both the bound-state and virtual-state poles approach to threshold, and they finally meet at the threshold around $N_C = 6$. By further increasing the values of N_C, the bound-state and virtual-state poles move into the complex plane on the second Riemann sheet and become a pair of resonance poles. At $N_C = 7$ we see a kink structure in the trajectories and by increasing N_C afterwards the resonance poles move deeper and deeper into the complex plane, with

increasing real and imaginary parts. The trajectory of $D_{s0}^*(2317)$ for large values of N_C is clearly different from the behavior of a standard quark-antiquark meson in QCD, which would fall down to the real axis with the mass behaving as a constant and the width scaling as $1/N_C$ [34]. In the left panel of Fig. 10, we show the N_C trajectories of the poles in the $(S, I) = (0, 1/2)$ case by considering the leading N_C scaling laws of h_i in Eq. (24). Compared to the $D_{s0}^*(2317)$ case in Fig. 9, the trajectories of the two poles in the $(S, I) = (0, 1/2)$ channel show a much simpler behavior. For large values of N_C, both the real and imaginary parts of the two poles tend to increase and they keep moving into the complex plane instead of falling down to the real axis. This behavior looks similar to that of the $D_{s0}^*(2317)$ for large values of N_C, indicating that the two charm scalar resonances with $(S, I) = (0, 1/2)$ do not seem to be a standard quark-antiquark meson at large N_C.

The previous N_C discussions are based on using the leading N_C scaling laws of the LECs h_i given in Eq. (24). In order to check the stability of our conclusions on the N_C
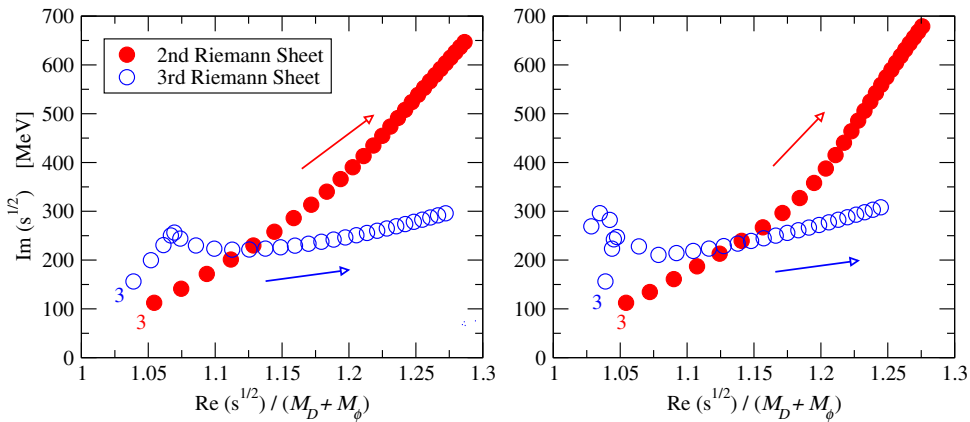

FIG. 10 (color online). N_c trajectories of the poles in the channel $(0, 1/2)$ with N_C varying from 3 to 30. The symbol ϕ in the horizontal-axis label is π for the 2nd RS, and η for the 3rd RS. Left: results with leading N_C scaling laws in Eq. (24); Right: results by including the subleading N_C scaling effects in Eqs. (26) and (27).

dependence of the poles, we follow Ref. [28] to include the subleading N_C scaling effects for the h_i. The explicit formulas read

$$h_i(N_c) = h_i(N_c = 3)$$
$$\times \left\{ 1 + \frac{h_i(N_c = 3) - h_i(N_c = \infty)}{h_i(N_c = 3)} \left(\frac{3}{N_c} - 1 \right) \right\},$$
$$i = 1, 3, 5 \qquad (26)$$

and

$$h_i(N_c) = \frac{3}{N_c} h_i(N_c = 3)$$
$$\times \left\{ 1 + \frac{h_i(N_c = 3) - h_i^{\text{Nor}}(N_c = \infty)}{h_i(N_c = 3)} \left(\frac{3}{N_c} - 1 \right) \right\},$$
$$i = 0, 2, 4, \qquad (27)$$

with the normalized h_i^{Nor} defined by $h_i^{\text{Nor}}(N_c = \infty) = \frac{N_c}{3} h_i(N_c = \infty)$. The fitted results of h_i in Table III can be considered as their values at $N_C = 3$. The quantities $h_i(N_c = \infty)$ in the previous formulas stand for their values at large N_C, which can be estimated from tree-level heavy resonance exchanges [50]. The resonance-saturation predictions of the h_i from Ref. [50] are

$$h_0(N_c = \infty) = 0, \quad h_2(N_c = \infty) = 0, \quad h_4'(N_c = \infty) = 0,$$
$$h_1(N_c = \infty) = 0.42, \quad h_3(N_c = \infty) = 2.23,$$
$$h_5'(N_c = \infty) = -1.45, \qquad (28)$$

which can be compared to our Fit-6C results

$$h_0 = 0.033, \quad h_2 = -0.08^{+0.29}_{-0.28}, \quad h_4' = -0.21^{+0.29}_{-0.27},$$
$$h_1 = 0.43, \quad h_3 = 3.79^{+0.38}_{-0.38}, \quad h_5' = -1.78^{+0.19}_{-0.19}.$$
$$(29)$$

As we can see, the resonance-saturation determinations are quite consistent with the Fit-6C results.

With the above preparations, we are at the point to study the influence of the subleading N_C scalings, specified by Eqs. (26), (27), on the determinations of the pole trajectories with varying N_C. The corresponding results together with the ones by only considering the leading N_C scalings, are shown in Figs. 9 and 10 for the $D_{s0}^*(2317)$ and the poles in the $(S, I) = (0, 1/2)$ channel, respectively. Qualitatively speaking, our conclusions based on the leading N_C scaling behaviors of h_i are not changed when including the subleading N_C effects. Taking the $D_{s0}^*(2317)$ trajectories for example, the only change is that the meeting point for the bound and virtual poles is at $N_C = 8$ in the case that the subleading N_C effects are included, while in the leading N_C case it happens at $N_C = 6$. But the trend of the pole

trajectories when increasing the values of N_C are almost the same in both cases. Similar conclusions can be also made for the poles in the $(S, I) = (0, 1/2)$ channel, as can be seen from Fig. 10.

The $1/N_C$ corrections of the subtraction constant a contributes another source of subleading N_C scaling effects. Since the subtraction constant is introduced through the unitarization procedure, it is rather difficult to directly estimate its leading N_C value, in contrast to the h_i situation. We simply vary the values of the scale μ in Eq. (19), but keeping the subtraction constant a fixed at its fitted value, to roughly estimate the subleading N_C scaling effects of a. Several different values of the μ from 0.9 GeV to 1.2 GeV are used to study the pole trajectories for the $D_{s0}^*(2317)$ and the $(S, I) = (0, 1/2)$ channel. Since we do not observe qualitative changes by using different values of μ and they look similar as the cases by introducing the subleading N_C scaling effects in the h_i, we shall not show explicitly these plots in order to avoid overloading the manuscript with too many figures.

V. CONCLUSIONS

In this work we have calculated the scattering of pNGBs (π, K, η, η') off charmed meson (D or D_s) and then unitarized the perturbative chiral amplitudes to investigate the charm scalar mesons. Recent lattice simulation data have been used in our study to constrain the free parameters in the fits. In addition to the prediction of the $D\pi$ scattering lengths with varying pion mass in the $(S, I) = (0, 1/2)$ channel, we also give predictions for all of the relevant scattering lengths with physical masses. Careful and extensive analyses of the charm scalar poles and their residues in different (S, I) channels have been carried out, which are summarized in Table VI. A virtual pole is found to be responsible for the positive scattering length in the $(S, I) = (-1, 0)$ channel. Two poles are observed for the $(S, I) = (1, 1)$ case: the one on the second sheet may explain the enhancement recently reported in Ref. [43]. The pole positions for the $D_{s0}^*(2317)$ and the channel with $(S, I) = (0, 1/2)$ are compatible with previous determinations, with the exception that our determination for the $(S, I) = (0, 1/2)$ pole at around 2.4 GeV has larger width, which is close to the PDG value. Both M_π and N_C trajectories for the $D_{s0}^*(2317)$ and the two poles in the $(S, I) = (0, 1/2)$ channel are studied in detail. The M_π trajectories of the pole around 2.1 GeV quite resembles the ones of the $f_0(500)$ obtained in Refs. [22,23]. The N_C trajectories of the $D_{s0}^*(2317)$ show that this physical bound state becomes a resonance for $N_C > 6$. For large values of N_C, the trajectories of the $D_{s0}^*(2317)$ and the poles with $(S, I) = (0, 1/2)$ do not tend to fall down to the real axis, indicating that they do not behave like the standard quark-antiquark mesons of QCD.

ACKNOWLEDGMENTS

APPENDIX: SOME OF THE COEFFICIENTS IN TABLE I

Here, we give the form of the coefficients in Table I that were not explicitly stated there:

$$C_1^{1,0\,DK\to D_s\eta} = \frac{-M_K^2(5c_\theta + 4\sqrt{2}s_\theta) + 3M_\pi^2 c_\theta}{2\sqrt{3}}, \tag{A1}$$

$$C_{35}^{1,0\,DK\to D_s\eta} = \frac{c_\theta + 2\sqrt{2}s_\theta}{\sqrt{3}}, \tag{A2}$$

$$C_0^{1,0\,D_s\eta\to D_s\eta}$$
$$= \frac{c_\theta^2(4M_K^2 - M_\pi^2) + 4\sqrt{2}c_\theta s_\theta(M_K^2 - M_\pi^2) + s_\theta^2(2M_K^2 + M_\pi^2)}{3}, \tag{A3}$$

$$C_1^{1,0\,D_s\eta\to D_s\eta} = \frac{2(M_\pi^2 - 2M_K^2)(\sqrt{2}c_\theta + s_\theta)^2}{3}, \tag{A4}$$

$$C_{35}^{1,0\,D_s\eta\to D_s\eta} = \frac{2(\sqrt{2}c_\theta + s_\theta)^2}{3}, \tag{A5}$$

$$C_1^{1,0\,DK\to D_s\eta'} = \frac{M_K^2(4\sqrt{2}c_\theta - 5s_\theta) + 3M_\pi^2 s_\theta}{2\sqrt{3}}, \tag{A6}$$

$$C_{35}^{1,0\,DK\to D_s\eta'} = \frac{s_\theta - 2\sqrt{2}c_\theta}{\sqrt{3}}, \tag{A7}$$

$$C_0^{1,0\,D_s\eta\to D_s\eta'} = \frac{2(M_\pi^2 - M_K^2)(\sqrt{2}c_\theta^2 - c_\theta s_\theta - \sqrt{2}s_\theta^2)}{3}, \tag{A8}$$

$$C_1^{1,0\,D_s\eta\to D_s\eta'} = \frac{2(2M_K^2 - M_\pi^2)(\sqrt{2}c_\theta^2 - c_\theta s_\theta - \sqrt{2}s_\theta^2)}{3}, \tag{A9}$$

$$C_{35}^{1,0\,D_s\eta\to D_s\eta'} = \frac{-2(\sqrt{2}c_\theta^2 - c_\theta s_\theta - \sqrt{2}s_\theta^2)}{3}, \tag{A10}$$

$$C_0^{1,0\,D_s\eta'\to D_s\eta'} = \frac{s_\theta^2(4M_K^2 - M_\pi^2) + 4\sqrt{2}c_\theta s_\theta(M_\pi^2 - M_K^2) + c_\theta^2(2M_K^2 + M_\pi^2)}{3}, \tag{A11}$$

$$C_1^{1,0\,D_s\eta'\to D_s\eta'} = \frac{2(M_\pi^2 - 2M_K^2)(\sqrt{2}s_\theta - c_\theta)^2}{3}, \tag{A12}$$

$$C_{35}^{1,0\,D_s\eta'\to D_s\eta'} = \frac{2(\sqrt{2}s_\theta - c_\theta)^2}{3}, \tag{A13}$$

$$C_0^{0,\frac{1}{2}\,D\eta\to D\eta} = \frac{c_\theta^2(4M_K^2 - M_\pi^2) + 4\sqrt{2}c_\theta s_\theta(M_K^2 - M_\pi^2) + s_\theta^2(2M_K^2 + M_\pi^2)}{3}, \tag{A14}$$

$$C_1^{0,\frac{1}{2}\,D\eta\to D\eta} = \frac{-M_\pi^2(\sqrt{2}s_\theta - c_\theta)^2}{3}, \tag{A15}$$

$$C_{35}^{0,\frac{1}{2}\,D\eta\to D\eta} = \frac{(\sqrt{2}s_\theta - c_\theta)^2}{3}, \tag{A16}$$

$$C_1^{0,\frac{1}{2}\,D_sK\to D\eta} = \frac{c_\theta(5M_K^2 - 3M_\pi^2) + 4\sqrt{2}s_\theta M_K^2}{2\sqrt{6}}, \tag{A17}$$

$$C_{35}^{0,\frac{1}{2}\,D_s K \to D\eta} = \frac{-(2\sqrt{2}s_\theta + c_\theta)}{\sqrt{6}}, \tag{A18}$$

$$C_0^{0,\frac{1}{2}\,D\eta \to D\eta'} = \frac{2(M_\pi^2 - M_K^2)(\sqrt{2}c_\theta^2 - c_\theta s_\theta - \sqrt{2}s_\theta^2)}{3}, \tag{A19}$$

$$C_1^{0,\frac{1}{2}\,D\eta \to D\eta'} = \frac{M_\pi^2(-\sqrt{2}c_\theta^2 + c_\theta s_\theta + \sqrt{2}s_\theta^2)}{3}, \tag{A20}$$

$$C_{35}^{0,\frac{1}{2}\,D\eta \to D\eta'} = \frac{(\sqrt{2}c_\theta^2 - c_\theta s_\theta - \sqrt{2}s_\theta^2)}{3}, \tag{A21}$$

$$C_1^{0,\frac{1}{2}\,D_s \overline{K} \to D\eta'} = \frac{(5M_K^2 - 3M_\pi^2)s_\theta - 4\sqrt{2}M_K^2 c_\theta}{2\sqrt{6}}, \tag{A22}$$

$$C_{35}^{0,\frac{1}{2}\,D_s \overline{K} \to D\eta'} = \frac{2\sqrt{2}c_\theta - s_\theta}{\sqrt{6}}, \tag{A23}$$

$$C_0^{1,0\,D\eta' \to D\eta'} = \frac{s_\theta^2(4M_K^2 - M_\pi^2) + 4\sqrt{2}c_\theta s_\theta(M_\pi^2 - M_K^2) + c_\theta^2(2M_K^2 + M_\pi^2)}{3}, \tag{A24}$$

$$C_1^{1,0\,D\eta' \to D\eta'} = \frac{-M_\pi^2(\sqrt{2}c_\theta + s_\theta)^2}{3}, \tag{A25}$$

$$C_{35}^{1,0\,D\eta' \to D\eta'} = \frac{(\sqrt{2}c_\theta + s_\theta)^2}{3}. \tag{A26}$$

---

[1] B. Aubert *et al.* (*BABAR* Collaboration), Observation of a Narrow Meson Decaying to $D_s^+ \pi^0$ at a Mass of 2.32-GeV/c², Phys. Rev. Lett. **90**, 242001 (2003).

[2] D. Besson *et al.* (CLEO Collaboration), Observation of a narrow resonance of mass 2.46-GeV/c² decaying to $D_s^+ \pi^0$ and confirmation of the $D_{sJ}^*(2317)$ state, Phys. Rev. D **68**, 032002 (2003).

[3] P. Krokovny *et al.* (Belle Collaboration), Observation of the D(sJ)(2317) and D(sJ)(2457) in B Decays, Phys. Rev. Lett. **91**, 262002 (2003).

[4] L. Liu, K. Orginos, F. K. Guo, C. Hanhart, and Ulf-G. Meißner, Interactions of charmed mesons with light pseudoscalar mesons from lattice QCD and implications on the nature of the $D_{s0}^*(2317)$, Phys. Rev. D **87**, 014508 (2013).

[5] D. Mohler, S. Prelovsek, and R. M. Woloshyn, $D\pi$ scattering and D meson resonances from lattice QCD, Phys. Rev. D **87**, 034501 (2013).

[6] D. Mohler, C. B. Lang, L. Leskovec, S. Prelovsek, and R. M. Woloshyn, $D_{s0}^*(2317)$ Meson and D-Meson-Kaon Scattering from Lattice QCD, Phys. Rev. Lett. **111**, 222001 (2013).

[7] C. B. Lang, L. Leskovec, D. Mohler, S. Prelovsek, and R. M. Woloshyn, Ds mesons with DK and D*K scattering near threshold, Phys. Rev. D **90**, 034510 (2014).

[8] A recent view: S. Aoki, Y. Aoki, C. Bernard, T. Blum, G. Colangelo, M. D. Morte, S. Drr, A. X. El Khadra *et al.*, Review of lattice results concerning low-energy particle physics, Eur. Phys. J. C **74**, 2890 (2014).

[9] G. Burdman and J. F. Donoghue, Union of chiral and heavy quark symmetries, Phys. Lett. B **280**, 287 (1992).

[10] M. B. Wise, Chiral perturbation theory for hadrons containing a heavy quark, Phys. Rev. D **45**, R2188 (1992).

[11] T. M. Yan, H. Y. Cheng, C. Y. Cheung, G. L. Lin, Y. C. Lin, and H. L. Yu, Heavy quark symmetry and chiral dynamics, Phys. Rev. D **46**, 1148 (1992); **55**, 5851(E) (1997).

[12] F. K. Guo, C. Hanhart, and U.-G. Meißner, Interactions between heavy mesons and Goldstone bosons from chiral dynamics, Eur. Phys. J. A **40**, 171 (2009).

[13] M. Altenbuchinger, L.-S. Geng, and W. Weise, Scattering lengths of Nambu-Goldstone bosons off D mesons and dynamically generated heavy-light mesons, Phys. Rev. D **89**, 014026 (2014).

[14] E. E. Kolomeitsev and M. F. M. Lutz, On heavy light meson resonances and chiral symmetry, Phys. Lett. B **582**, 39 (2004).

[15] J. Hofmann and M. F. M. Lutz, Open charm meson resonances with negative strangeness, Nucl. Phys. **A733**, 142 (2004).

[16] F. K. Guo, P. N. Shen, H. C. Chiang, R. G. Ping, and B. S. Zou, Dynamically generated 0^+ heavy mesons in a heavy chiral unitary approach, Phys. Lett. B 641, 278 (2006).

[17] M. Altenbuchinger and L. S. Geng, Off-shell effects on the interaction of Nambu-Goldstone bosons and D mesons, Phys. Rev. D 89, 054008 (2014).

[18] M. Cleven, F. K. Guo, C. Hanhart, and U.-G. Meißner, Light meson mass dependence of the positive parity heavy-strange mesons, Eur. Phys. J. A 47, 19 (2011).

[19] P. Wang and X. G. Wang, Study on 0^+ states with open charm in unitarized heavy meson chiral approach, Phys. Rev. D 86, 014030 (2012).

[20] L. S. Geng, N. Kaiser, J. Martin-Camalich, and W. Weise, Low-energy interactions of Nambu-Goldstone bosons with D mesons in covariant chiral perturbation theory, Phys. Rev. D 82, 054022 (2010).

[21] D. L. Yao, M. L. Du, F. K. Guo, and U.-G. Meißner, One-loop analysis of the interactions between charmed mesons and Goldstone bosons, arXiv:1502.05981.

[22] C. Hanhart, J. R. Pelaez, and G. Rios, Quark Mass Dependence of the Rho and Sigma from Dispersion Relations and Chiral Perturbation Theory, Phys. Rev. Lett. 100, 152001 (2008).

[23] C. Hanhart, J. R. Pelaez, and G. Rios, Remarks on pole trajectories for resonances, Phys. Lett. B 739, 375 (2014).

[24] Z. X. Sun, L. Y. Xiao, Z. Xiao, and H. Q. Zheng, Model dependent analyses on the N(c) dependence of the sigma pole trajectory, Mod. Phys. Lett. A 22, 711 (2007).

[25] J. R. Pelaez and G. Rios, Nature of the f0(600) from its N(c) Dependence at Two Loops in Unitarized Chiral Perturbation Theory, Phys. Rev. Lett. 97, 242002 (2006).

[26] L. Y. Dai, X. G. Wang, and H. Q. Zheng, Pole analysis on unitarized $SU(3) \times SU(3)$ one loop χPT amplitudes, Commun. Theor. Phys. 57, 841 (2012).

[27] Z. H. Guo and J. A. Oller, Resonances from meson-meson scattering in U(3) CHPT, Phys. Rev. D 84, 034005 (2011).

[28] Z. H. Guo, J. A. Oller, and J. R. de Elvira, Chiral dynamics in form factors, spectral-function sum rules, meson-meson scattering and semi-local duality, Phys. Rev. D 86, 054006 (2012).

[29] A. Martinez Torres, E. Oset, S. Prelovsek, and A. Ramos, Reanalysis of lattice QCD spectra leading to the $D_{s0}^*(2317)$ and $D_{s1}^*(2460)$, J. High Energy Phys. 05 (2015) 153.

[30] D. Agadjanov, F.-K. Guo, G. Rios, and A. Rusetsky, Bound states on the lattice with partially twisted boundary conditions, J. High Energy Phys. 01 (2015) 118.

[31] E. Witten, Current algebra theorems for the U(1) "Goldstone boson", Nucl. Phys. B156, 269 (1979).

[32] S. Coleman and E. Witten, Chiral-symmetry breakdown in large-N Chromodynamics, Phys. Rev. Lett. 45, 100 (1980).

[33] G. Veneziano, U(1) without instantons, Nucl. Phys. B159, 213 (1979).

[34] A. V. Manohar, Large N QCD, arXiv:hep-ph/9802419.

[35] J. Gasser and H. Leutwyler, Chiral perturbation theory: Expansions in the mass of the strange quark, Nucl. Phys. B250, 465 (1985).

[36] R. Kaiser and H. Leutwyler, Large N(c) in chiral perturbation theory, Eur. Phys. J. C 17, 623 (2000).

[37] P. Herrera-Siklody, J. I. Latorre, P. Pascual, and J. Taron, Chiral effective Lagrangian in the large N(c) limit: The nonet case, Nucl. Phys. B497, 345 (1997).

[38] J. A. Oller and E. Oset, N/D description of two meson amplitudes and chiral symmetry, Phys. Rev. D 60, 074023 (1999).

[39] J. A. Oller and U.-G. Meißner, Chiral dynamics in the presence of bound states: Kaon nucleon interactions revisited, Phys. Lett. B 500, 263 (2001).

[40] X. K. Guo, Z. H. Guo, J. A. Oller, and J. J. Sanz-Cillero, Scrutinizing the eta-eta' mixing, masses and pseudoscalar decay constants in the framework of U(3) chiral effective field theory, J. High Energy Phys. 06 (2015) 175.

[41] C. Michael, K. Ottnad, and C. Urbach, η and η' Mixing from Lattice QCD, Phys. Rev. Lett. 111, 181602 (2013).

[42] L. Liu, H.-W. Lin, and K. Orginos, Charmed hadron interactions, Proc. Sci., LATTICE2008 (2008) 112 [arXiv:0810.5412].

[43] M. V. Purohit, Dalitz plot analysis of $B \to DDK$ decays, arXiv:1506.00600.

[44] K. A. Olive et al. (Particle Data Group Collaboration), Review of particle physics, Chin. Phys. C 38, 090001 (2014).

[45] J. R. Pelaez and G. Rios, Light scalar mesons: Comments on their behavior in the $1/N(c)$ expansion near $N(c) = 3$ versus the $N(c) \to$ infinity limit, Acta Phys. Polon. Supp. 2, 215 (2009).

[46] H. Nagahiro, K. Nawa, S. Ozaki, D. Jido, and A. Hosaka, Composite and elementary natures of $a_1(1260)$ meson, Phys. Rev. D 83, 111504 (2011).

[47] G. 't Hooft, A planar diagram theory for strong interactions, Nucl. Phys. B72, 461 (1974).

[48] E. Witten, Baryons in the $1/n$ expansion, Nucl. Phys. B160, 57 (1979).

[49] S. Weinberg, The U(1) problem, Phys. Rev. D 11, 3583 (1975).

[50] M.-L. Du, F.-K. Guo, U.-G. Meißner, and D.-L. Yao (to be published).